



Abrupt Common Era hydroclimate shifts drive west Greenland ice cap change

Matthew B. Osman^{1,2}✉, Benjamin E. Smith³, Luke D. Trusel^{1,4}, Sarah B. Das⁵, Joseph R. McConnell^{1,6}, Nathan Chellman⁶, Monica Arienzo⁶ and Harald Sodemann⁷

Ice core archives are well suited for reconstructing rapid past climate changes at high latitudes. Despite this, few records currently exist from coastal Greenlandic ice caps due to their remote nature, limiting our long-term understanding of past maritime and coastal climate variability across this rapidly changing Arctic region. Here, we reconstruct regionally representative glacier surface mass balance and climate variability over the last two thousand years (-169–2015 ce) using an ice core collected from the Nuussuaq Peninsula, west Greenland. We find indications of abrupt regional hydroclimate shifts, including an up to 20% decrease in average snow accumulation during the transition from the Medieval Warm Period (950–1250 ce) to Little Ice Age (1450–1850 ce), followed by a subsequent >40% accumulation increase from the early 18th to late 20th centuries ce. These coastal changes are substantially larger than those previously reported from interior Greenland records. Moreover, we show that the strong relationship observed today between Arctic temperature rise and coastal ice cap decay contrasts with that of the last millennium, during which periods of warming led to snowfall-driven glacial growth. Taken together with modern observations, the ice core evidence could indicate a recent reversal in the response of west Greenland ice caps to climate change.

Satellite observations¹, ice core records² and climate models³ have revealed accelerating mass loss of the Greenland Ice Sheet (GrIS) during recent decades, as well as widespread thinning, receding and speeding up of Greenland's marine-terminating outlet glaciers⁴. These glaciological changes directly contribute to global sea level rise⁵, impacting ocean overturning⁶ and marine ecosystems downstream^{7,8}. Yet whereas such observations highlight the sensitivity of the GrIS to industrial-era Arctic warming^{9,10}, especially across daily to interannual timescales^{3,4}, little is known of the long-term (multidecadal to centennial) response of Greenland's marginal environments and its peripheral glaciers and ice caps (GICs) to climatic forcing. Given recent findings that GICs accounted for upwards of 20% of Greenlandic ice losses during the early 21st century (despite encompassing less than 5% of the GrIS area^{11,12}), it is important to reconcile such uncertainties by placing contemporary GIC observations into a longer-term perspective.

Naturally derived climate proxies offer the potential to extend our understanding of past GIC-climate coupling well beyond the satellite era. However, existing records are limited in scope and, in many regions, provide conflicting information. Across the climatically sensitive coastal west Greenland (CWG) and northeastern Canadian Arctic regions (Fig. 1a), for example, recent studies using proglacial sediments^{13–15} and mosses^{15,16} have provided critical age constraints on the timing of GIC expansion during the previous two millennia. These studies reveal intervals of glacier advancement during the Medieval Warm Period (MWP), a period of widespread relative warmth, as well as during the colder Little Ice Age (LIA). By assuming that GIC growth primarily coincides with declining summertime temperatures, such findings have given rise to the notion that 'paradoxical' (that is, relatively cool) climate conditions existed across CWG and northeastern Canada during the MWP^{13–15}. However, evi-

dence from coeval temperature-specific proxy records from CWG lake and marine sediment core sites is inconclusive; results are either consistent^{16,17} or inconsistent^{18–20} with this suggestion depending on the particular record, location or proxy referenced (Extended Data Fig. 1). Such ambiguity, likely related in part to coarse proxy resolution and imprecise dating (Extended Data Fig. 1), represents an outstanding limitation of our ability to understand the fundamental response of coastal Greenland GICs to long-term climate change.

In spring 2015 we recovered an ice core allowing for direct and internally consistent insights into coupled climate-GIC variability over the Common Era via its high-resolution history of past snow accumulation in CWG. Extracted from a cold-based, high-elevation ice cap perched atop the Nuussuaq Peninsula, west Greenland (70.49°N, 52.26°W, ~2,010 metres above sea level), the 'NU' record is, to our knowledge, the only continuous and precisely dated (Methods) millennium-scale ice core from the western Greenlandic seaboard (Fig. 1a), rendering it well suited for re-evaluating pre-observational coastal climate and glacial variability. Here, we describe the methodology used to date the NU core, including use of an observationally constrained ice strain inversion method developed herein allowing for our reconstruction of past snow accumulation. Using this record, we explore the influences underlying CWG hydroclimate variability and GIC growth, highlighting the first-order influence of regional surface temperatures on coastal snowfall changes.

Core dating and ice strain inversion

The NU ice core was drilled to a depth of approximately 138 metres below the surface, shy of bedrock at a location marginally downslope of the ice cap summit (Fig. 2a, Methods and Supplementary Sections 1–4). Chemical measurements, conducted continuously and at high

¹Massachusetts Institute of Technology/Woods Hole Oceanographic Institution Joint Program in Oceanography/Applied Ocean Sciences and Engineering, Woods Hole, MA, USA. ²Department of Geosciences, University of Arizona, Tucson, AZ, USA. ³Applied Physics Laboratory, University of Washington, Seattle, WA, USA. ⁴Department of Geography, Pennsylvania State University, University Park, PA, USA. ⁵Department of Geology and Geophysics, Woods Hole Oceanographic Institution, Woods Hole, MA, USA. ⁶Division of Hydrologic Sciences, Desert Research Institute, Reno, NV, USA. ⁷Geophysical Institute, University of Bergen and Bjerknes Centre for Climate Research, Bergen, Norway. ✉e-mail: mattosman@arizona.edu

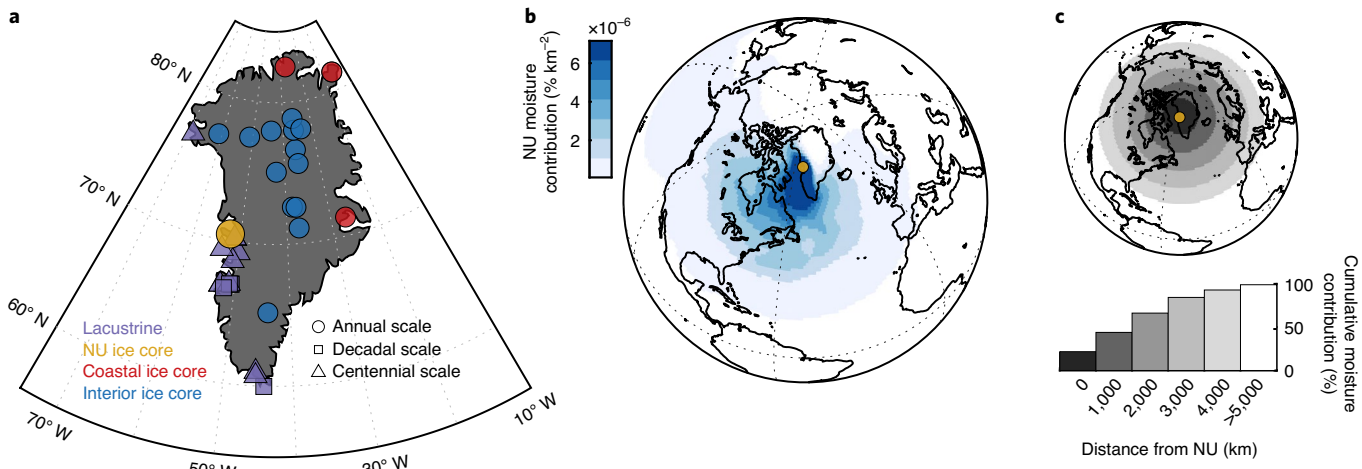


Fig. 1 | Nuussuaq ice cap location and moisture source influences. **a**, Previously analysed coastal (red) and interior (blue) Greenlandic ice core sites whose record lengths extend beyond the last millennium. The yellow dot denotes the NU ice cap location. Locations of terrestrial temperature proxy records containing >10 data points during the last millennium are shown in purple (Extended Data Fig. 1). **b**, Percent contribution per kilometre squared of the annual NU precipitation budget, inferred from a Lagrangian moisture source diagnostic (Methods). Note that the global area integral of **b** is 100%. **c**, Cumulative moisture contribution from **b** as a function of radial distance from the NU ice core site.

resolution²¹, permitted identification of 55 age-constraint tie-points over the span of the core length (Methods). These tie-points reference 20th century radiogenic bomb horizons, volcanic eruptions and anthropogenically sourced heavy-metal emissions (Fig. 2b and Extended Data Fig. 2) and reveal the NU record to cover an age range of approximately 169 to 2015 CE.

Leveraging the advantageous physical setting of the NU ice cap (Methods), we developed a one-dimensional, physically based ice strain inversion method in order to both (1) refine our preliminary age scale and (2) establish an accumulation history for the NU ice cap (**m**, hereafter denoting the annual net surface mass balance, the difference between annually accumulated snowfall minus sublimation and summertime surface meltwater runoff), relying on the 55 age tie-points observed along the core length. Specifically, our approach sought an accumulation history (**m**) that is both ‘simple’ (denoting minimal deviations in accumulation rate from the NU site’s climatological mean) and consistent with our tie-point observations (Fig. 2b), thus minimizing the cost function (J):

$$J(\mathbf{m}, \dot{b}_0, H_0) = \left\| \frac{G(\mathbf{m}, \dot{b}_0, H_0) - \mathbf{d}}{\sigma} \right\|^2 + \lambda \|\mathbf{s} - 1\|^2. \quad (1)$$

Here, \dot{b}_0 is the site-representative climatological accumulation rate, and H_0 is the site ice cap thickness. The function $G(\mathbf{m}, \dot{b}_0, H_0)$ represents layer-age estimates from a forward one-dimensional ice flow model (Methods) that maps our accumulation history onto an idealized depth-age scale assuming only steady-state \dot{b}_0 and H_0 conditions, whereas the vector \mathbf{d} contains the 55 observed age-constrained depths; the difference between the two is normalized by the observed depth uncertainties (σ). The weight value λ specifies the relative importances of the layer thicknesses and the data misfits in determining J , conditioning the ill-constrained problem for uniqueness, while \mathbf{s} represents a set of scaling values that quantify the ratio between \mathbf{m} and \dot{b}_0 for each year in the model. All double-barred terms in equation (1) denote the standard (Euclidian) norm. Minimizing the first term of equation (1) improves the match between the time-depth scale at the data points, while minimizing the second term yields a simpler ice strain history; minimizing both

gives a solution that balances the two, the exact solution being dictated by the choice of λ (Supplementary Section 5).

We used a two-dimensional grid search to minimize J across a range of H_0 (120 to 165 m ice eq.) and \dot{b}_0 (0.2 to 0.45 m_{ice} yr⁻¹) reference values (equation (1)), assuming constant (that is, stepwise) **m** between observations (**d**). This procedure revealed a ‘minimum complexity’ model (that is, most simple and consistent **m**) at $\dot{b}_0 = 0.325$ m_{ice} yr⁻¹ and $H_0 = 141$ m_{ice} (Fig. 3a and Extended Data Figs. 3 and 4), the latter being only one metre thinner than an independent field-derived estimate based on radar measurements and the density-depth profile (Fig. 2 and Supplementary Section 2). While we thus expect that our least complex variation indicates accurate values of \dot{b}_0 and H_0 , we also acknowledge that models slightly more complex than the minimum need not necessarily be incorrect. Given this fact, we nominally prescribed the distribution of accumulation models whose complexity was no more than 10% larger than that of the least complex model as ‘acceptable’ and indicative of the uncertainty in our dating process. These values delineate a skewed ellipse, with acceptable ice cap thicknesses (H_0) between 138 and 144 m_{ice} and acceptable reference accumulation rates (\dot{b}_0) between 0.30 and 0.35 m_{ice} yr⁻¹ (Fig. 3a). The recovered NU accumulation histories for all such models are provided in Fig. 3b, each showing broad agreement, albeit with increasing divergence (that is, relative uncertainty) at progressively deeper depths (that is, older portions) of the NU core. Importantly, however, the same relative patterns of centennial-scale accumulation variability occur even across less acceptable models, especially during the last millennium (Extended Data Fig. 4).

Abrupt hydroclimate shifts over the Common Era

Our reconstructed NU accumulation record reveals abrupt changes in CWG hydroclimate conditions across the Common Era, with climatological accumulation decreases averaging upwards of 20% moving out of the late MWP (13th century) into the height of the LIA (17th century) followed by a subsequent ~45% increase moving from the LIA into contemporary industrial-era conditions (late 20th century; Fig. 4b). These accumulation changes are substantially larger than last-millennium accumulation changes previously reported^{22,23} across the interior GrIS (Fig. 4e), highlighting both the enhanced sensitivity of CWG hydroclimate variability to large-scale

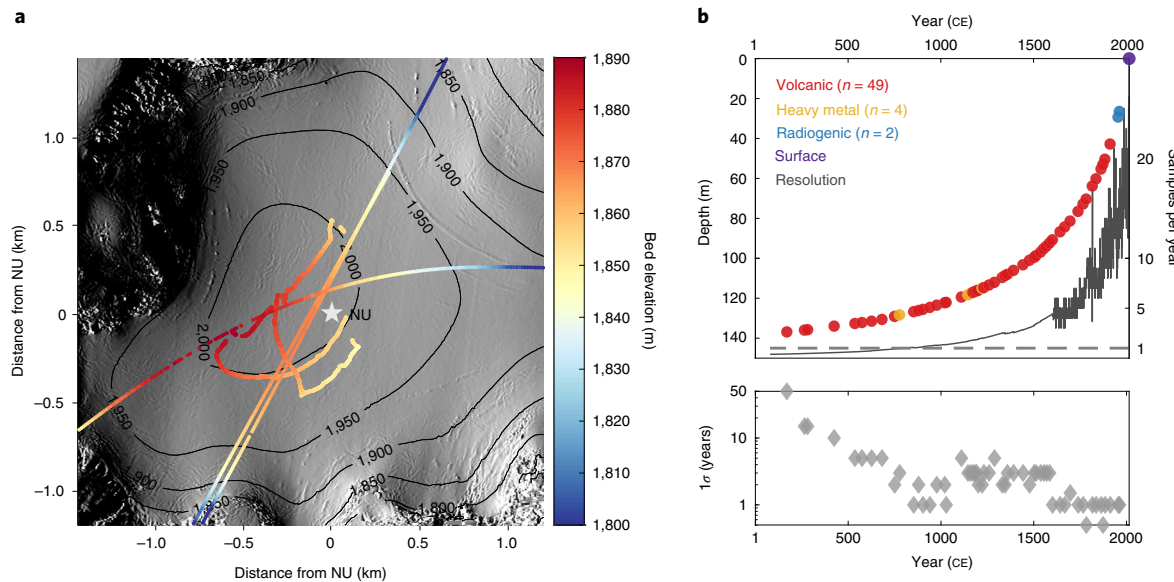


Fig. 2 | Nuussuaq ice cap glaciological setting and estimated ice core age constraints. **a**, Map of the sampling location showing a digital elevation model (black contours; labels indicate bed elevation in metres) derived from the Worldview-1 stereophotogrammetry (DigitalGlobe imagery) and bed-elevation measurements (metres above sea level) derived from our 2014 ground-based radar survey (irregular lines near sampling location) and three NASA Operation Ice Bridge airborne-radar transects (long, smooth lines; Supplementary Sections 2 and 3). The NU ice core site ($70.49^{\circ}\text{N}, 52.26^{\circ}\text{W}$) is shown by a white star, where bedrock depth is indicated at -153 ± 10 m; Supplementary Information). **b**, Top panel: age constraints for the NU core versus depth (left axis), with chemistry-sampling resolution (grey line, right axis; note dashed line denotes the one-year resolution sampling limit). Annual layer counting (>3 samples per year at a nominal sampling rate of ~ 2 cm water equivalents per sample) was possible to 1601 ce. Bottom panel: corresponding 1σ age uncertainties in the depth-age constraints.

climatic shifts during the last millennium and the exceptional ability of the NU ice cap (and likely Greenland GICs more generally) to respond to, and hence record, climate variability. Indeed, we find strong covariation ($r=0.70$, $P < 0.001$; P here and throughout determined via the method of Ebisuzaki²⁴) between our NU accumulation record and reconstructed Arctic 2k surface temperatures²⁵ based predominantly on terrestrial proxies from northeast Canada and Greenland (Fig. 4c), an association not exhibited by interior ice core accumulation records^{22,23,26}. Similarly strong coupling also extends into the recent industrial era (~ 1840 –1980; $r=0.69$, $P < 0.001$), when comparison with nearby CWG meteorological measurements is possible (Extended Data Fig. 5). The relative insensitivity of interior GrIS hydroclimate conditions to temperature, in turn, has been noted elsewhere^{27,28} and may be linked to higher moisture content variations at low-elevation coastal sites²⁸, localized sea ice influences²⁹ or seasonal differences in moisture source, evaporation or transport³⁰.

To better constrain the hydroclimatic links relating our NU accumulation record to regional changes (namely, surface temperature and sea ice cover), we conducted Lagrangian-based analysis of moisture transport variability to the NU ice cap at high resolution (6-hourly) over a multidecadal timeframe (1980–2013; Methods) using the state-of-the-art WaterSip^{30,31} moisture source accounting model. Model results point to the dominance of regional moisture sources from Baffin Bay and northeastern Canada for snowfall precipitated atop the Nuussuaq ice cap (Fig. 1b,c and Extended Data Fig. 6) and confirm the NU record as well poised for inferring past hydroclimatic conditions along the CWG margin and Baffin Bay maritime province more broadly. These results further corroborate a significant positive link ($P < 0.001$) between modelled NU precipitation and regional temperature variations across monthly to interannual timescales (Extended Data Fig. 7a,b). In turn, NU precipitation versus Baffin Bay sea ice extent anomalies exhibit comparably weak, albeit non-negligible, mean annual association

($P=0.077$) during recent decades (Extended Data Fig. 7c). In particular, although persistent sea ice coverage can negatively influence NU precipitation during late-winter months (ostensibly by controlling the area of open ocean exposed to evaporation), interannual variations in CWG precipitation appear most sensitive to changes in marine evaporation during late summer when precipitation is maximum and sea ice cover absent across Baffin Bay (Extended Data Figs. 6a,b and 8). Given the Common Era-long stability in CWG precipitation seasonality shown by a recent lake-derived leaf-wax reconstruction¹⁹, our moisture source analyses thus imply that regional surface temperature changes remained the dominant influence on NU accumulation throughout the span of our record.

Our finding that Common Era changes in NU ice cap accumulation roughly scaled with regional temperature prior to extensive late-20th-century GIC mass loss rates also provides better constraints on Greenlandic GIC sensitivity, critical for modelling initiatives previously limited to interior GrIS proxy records^{26,32}. While temperature-dependent scaling of snow accumulation is consistent with expectations from the Clausius–Clapeyron relation^{29,33}, the strong covariance with regional pre-21st century temperature change exhibited by our record is distinct from pre-existing interior GrIS records that decouple from Clausius–Clapeyron below multimillennial timescales^{22,23,26}. Our moisture source analysis suggests an enhanced CWG precipitation sensitivity of $0.032 \pm 0.007 \text{ m}_{\text{ice}} \text{ yr}^{-1}$ per degree centigrade moisture source warming, a value in close alignment with independent estimates of NU accumulation sensitivity based on nearby meteorological measurements and an ensemble of pan-Arctic reanalyses (Extended Data Fig. 9).

Contextualizing past and present coastal ice cap changes

The significant positive association between Common Era NU accumulation and regional temperature change also offers an alternative explanation of several prior reconstructions of glacial

advance across the greater Baffin Bay region during the MWP, in lieu of the paradoxical MWP climate conditions argued for elsewhere^{13–16}. Notably, Young et al.¹³, Jomelli et al.¹⁴ and Schweinsberg et al.¹⁵ each used independent cosmogenic-nuclide-exposure moraine-dating methods to infer centennial-scale positioning in nearby Nuussuaq Peninsula, Disko Island and (latitudinally adjacent) eastern Baffin Island outlet glacier termini, with each study concluding that regional outlet glaciers reached or approached their most advanced Common Era states during the classical peak of the MWP (10th to 13th centuries), prior to LIA cooling (Fig. 4a). Glaciers advance during times of persistent positive mass balance, generally as a result of a reduction in summertime temperature limiting melt and/or an increase in accumulation causing growth³⁴. In the absence of prior coastal accumulation histories and the stable accumulation history shown by interior GrIS records (Fig. 4e), these studies interpreted advanced MWP glacial termini positions as representing prevailing (and thus paradoxical) regional cold conditions that limited summertime coastal GIC melt, possibly due to a purported positive persistence³⁵ of the North Atlantic Oscillation (NAO) during the MWP. The NAO is a climate pattern denoting shifting of the sea level pressure dipole over Iceland and Azores that, during its positive phase, manifests as surface cooling across north-east Canada and Greenland (Extended Data Fig. 10b).

By contrast, our coastal ice cap accumulation record implies that advanced regional glacier termini positions during the MWP more likely arose from the strong positive influence of temperature on regional precipitation. In this case, increases in surface temperature during the MWP would have enhanced both local and far-field moisture uptake (Fig. 1b), increasing coastal snowfall rates, facilitating ice cap accumulation gains at high elevations and, eventually, the advancement of lower-elevation glacial termini over multiple decades to centuries. While we acknowledge that such increases in MWP temperatures would have likely also increased summertime mass losses across low-elevation ablation areas, such losses were probably limited prior to enhanced late-20th-century surface warming and possibly attenuated by increased snowfall that could further mitigate melt-based losses by both suppressing the melt-albedo feedback³ and enhancing melt retention rates via firn replenishment³⁶. Supporting this suggestion, we highlight a compilation of regional ice core melt records³⁷ alongside the NU melt record² (Fig. 4d and Extended Data Fig. 5i). Despite these records' differing melt-temperature-elevation dependencies, each indicates similar MWP melt levels that, while on average elevated relative to LIA levels, are strongly suppressed relative to post-industrial warming owing to the non-linear melt-temperature sensitivity². As coastal ice core melt records have been shown to provide spatially extensive insights into past GIC meltwater runoff rates throughout this region², these data imply that regional ablation area mass losses during the MWP were only marginally higher than LIA levels (and thus viably compensated by increased high-elevation snowfall; Fig. 4b).

Given the sensitivity of CWG GICs to summertime NAO phasing shown by observations^{1,38} and models^{39,40}, we cannot definitively rule out the possibility that the persistent positive NAO state³⁵ championed by prior authors^{13–15} also served as a mechanism for MWP GIC growth. However, notwithstanding more recent proxy^{41–43} and modelling-based analyses^{42,44} that have refuted the notion of a persistently positive MWP NAO³⁵, this hypothesis would imply that temperature-sensitive proxies across Greenland and northeastern Canada should also exhibit signatures of cooling during the MWP (Young et al.¹³ and Extended Data Fig. 10b). Yet this does not appear to be the case: the MWP-warm to LIA-cold transition is a defining feature of the Arctic 2k reconstruction²⁵ (Fig. 4c), itself featuring a well-vetted surface temperature proxy compilation strongly reflecting Baffin Bay changes (Extended Data Fig. 10b). Similarly, near-unambiguous inferences of enhanced summertime melt from our Baffin Bay ice core compilation (Fig. 4e) support MWP warmth,

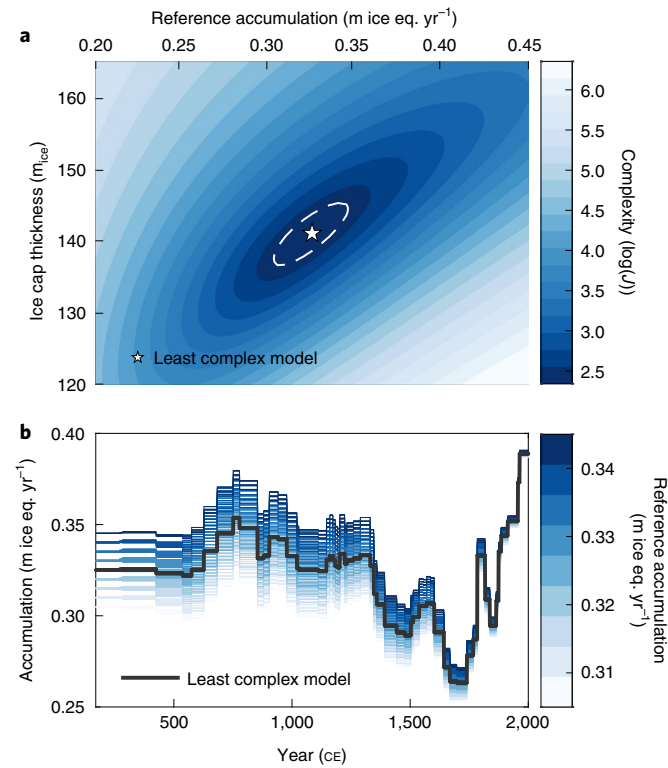


Fig. 3 | Optimum reconstruction of past Nuussuaq ice cap accumulation changes. **a**, Model complexity (J values) for refined age-depth scales over a range of ice cap thicknesses (H_0) and climatological reference accumulation (b_0) values. The white-dashed contour denotes models that are ~10% more complex than the 'optimum' least complex model (white star). **b**, Recovered NU accumulation histories for models less than 10% more complex than the optimum model. Each history is coloured by its reference accumulation value. There is notable consistency in the timing and relative magnitude of last-millennium accumulation changes across the full range of recovered histories.

as do near-direct estimates of past temperature measured directly from GrIS boreholes⁴⁵ and a $\delta^{15}\text{N}$ - and $\delta^{40}\text{Ar}$ -gas-derived temperature reconstruction⁴⁶ from Summit, Greenland (Extended Data Fig. 10a). Overall, the sum of available evidence showing MWP warmth, including new analyses presented here, negates a persistent positive NAO state as necessary to invoke MWP GIC mass gains, despite limited, and less direct, evidence suggestive of the contrary^{13–15,17,47} (Extended Data Figs. 1 and 10a).

From this conclusion, however, naturally arises the following paradox: if warming has tended to induce GIC growth in CWG during periods of the past, why have glaciers in this region largely receded from their LIA positions during the industrial era¹⁵? While our ice-core-based reconstruction alone cannot definitively reconcile this question, it is widely accepted that both the rate and magnitude of recent warming in this region have greatly exceeded those arising from natural variability during the last millennium^{9,25} (Fig. 4c). In CWG, widespread outlet glacier recession commenced by the early to mid-20th century⁴⁸, a timeframe that lags the estimated onset of industrial-era warming of this region⁹ by as much as six to ten decades but is broadly consistent with the exceedance of regional temperatures beyond MWP levels (Fig. 4c). Due to the strongly non-linear and threshold-limited^{2,3} response of Greenland GICs to climate, further warming of this region during subsequent decades of the mid to late 20th century may have accelerated CWG outlet glacier recession^{15,48} while associated ice cap accumulation zones situated at higher altitudes continued to gain mass from

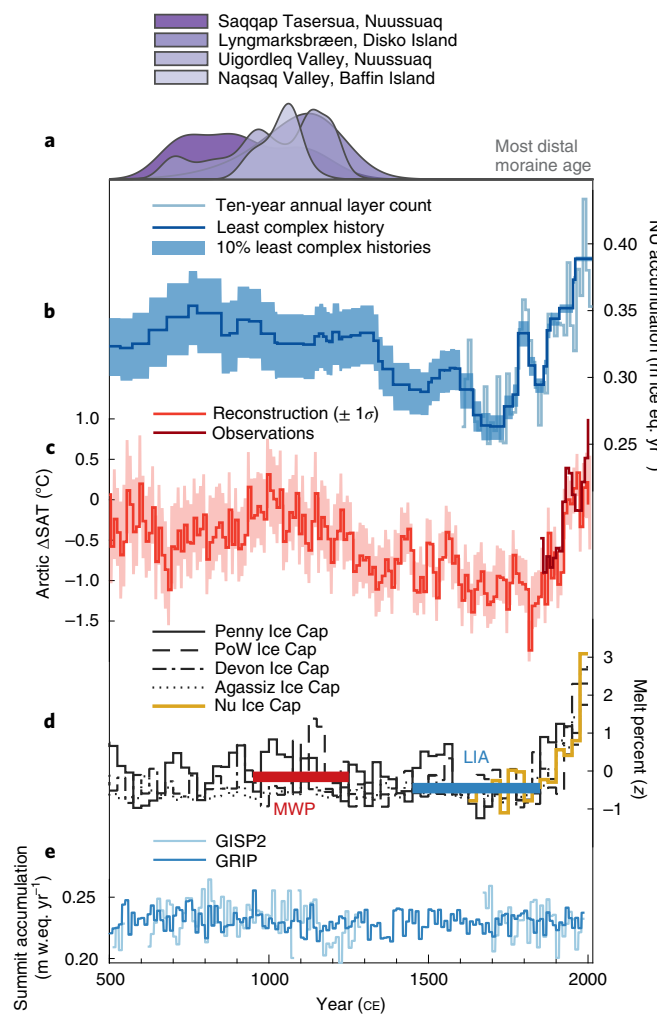


Fig. 4 | Enhanced sensitivity in Nuussuaq ice cap accumulation to last-millennium climate variability. **a**, CWG and Baffin Island ‘most distal’ moraine age probability density functions from Young et al.¹³, Jomelli et al.¹⁴ and Schweinsberg et al.¹⁵. The terminology ‘most distal’ refers to the most advanced Common Era glacier terminus moraine identified at each site^{13–15}. **b**, The optimum NU accumulation history with the 10% least complex interval. Superimposed is the ten-year mean NU accumulation history from annual layer counting. **c**, The multiproxy Arctic 2k surface air temperature (SAT) reconstruction²⁵ overlain with observations from HadCRUT4 (ref. ⁵⁰). **d**, Compilation of ice core melt percentage records from northeastern Canada³⁷ and the NU ice core melt history of Trusel et al.², each unit-normalized to their overlapping period. Regional average melt rates during the MWP and LIA are shown by the red and blue lines, respectively. **e**, Previously reported^{22,23} accumulation histories for Summit, Greenland, illustrating the comparably low sensitivity of interior GrIS hydroclimate changes to regional temperature variability.

increased snowfall. Such conditions are suggested by our NU ice core accumulation record, which shows significant ($P < 0.001$) positive covariation with local annual and summertime air temperatures over much of the industrial era (Extended Data Fig. 5f,g) as coeval recession of nearby low-lying outlet glaciers ensued^{13,15}.

Under continued anthropogenic warming, the tenacity of high-elevation CWG ice cap accumulation zones becomes less clear: models predict that GIC accumulation areas such as NU have recently (or will soon) become subject to threshold-like tipping points due to accelerating summertime melt rates exceeding annual snowfall^{2,49}. In particular, increased melt frequency is shown

to invoke a positive mass loss feedback that diminishes the buffering capacity of these GICs’ firn layers to refreeze surface meltwater³ while also increasing the occurrence of near-impermeable ice layers that accelerate runoff⁴⁶ and decrease albedo³. Indeed, our annually resolved NU accumulation record hints at an anomalous negative trend during the most recent two to three decades of rising coastal temperatures (Extended Data Fig. 5e–g), coinciding with the emergence of regional ice cap surface melt to levels unprecedented over the preceding centuries to, possibly, millennia^{2,37}. This could indicate an ongoing regional shift from a positive (snowfall-driven) to negative (melt-driven) temperature–mass balance GIC regime.

In summary, our NU ice core accumulation record demonstrates an enhanced sensitivity of CWG ice caps to regional hydroclimate variability (Fig. 4 and Extended Data Figs. 5 and 7–10). We illustrate a near-linear positive coupling between NU ice cap mass balance and regional temperature change across much of the Common Era, a finding that stands in contrast to the negative relationship observed across most Greenland glaciers today and predicted under future warming scenarios^{2,3,49}. Critically, our reconstruction rebuts suggestions of paradoxical climate conditions in CWG during the last millennium^{13–16}, offering instead a more nuanced view of the interplay between temperature, snowfall and GIC responses to a warming Arctic that may have important implications for future sea level rise^{11,12}. Nonetheless, the apparent Common Era scalability between temperature and CWG accumulation is unlikely to remain stationary given recent rapid Arctic warming above the range of natural variability⁹. Continued monitoring and future modelling work across a range of coastal GICs will help better quantify the counteracting relationship between warming-induced increases in snowfall and accelerating ice cap melt.

Online content

Any methods, additional references, Nature Research reporting summaries, source data, extended data, supplementary information, acknowledgements, peer review information; details of author contributions and competing interests; and statements of data and code availability are available at <https://doi.org/10.1038/s41561-021-00818-w>.

Received: 12 August 2020; Accepted: 19 July 2021;

Published online: 9 September 2021

References

1. Bevis, M. et al. Accelerating changes in ice mass within Greenland, and the ice sheet’s sensitivity to atmospheric forcing. *Proc. Natl Acad. Sci. USA* **116**, 1934–1939 (2019).
2. Trusel, L. D. et al. Nonlinear rise in Greenland runoff in response to post-industrial Arctic warming. *Nature* **564**, 104–108 (2018).
3. Noël, B. et al. A tipping point in refreezing accelerates mass loss of Greenland’s glaciers and ice caps. *Nat. Commun.* **8**, 14730 (2017).
4. Moon, T., Joughin, I., Smith, B. & Howat, I. 21st-century evolution of Greenland outlet glacier velocities. *Science* **336**, 576–578 (2012).
5. Mouginot, J. et al. Forty-six years of Greenland Ice Sheet mass balance from 1972 to 2018. *Proc. Natl Acad. Sci. USA* **116**, 9239–9244 (2019).
6. Böning, C. W., Behrens, E., Biastoch, A., Getzlaff, K. & Bamber, J. L. Emerging impact of Greenland meltwater on deepwater formation in the North Atlantic Ocean. *Nat. Geosci.* **9**, 523–527 (2016).
7. Arrigo, K. R. et al. Melting glaciers stimulate large summer phytoplankton blooms in southwest Greenland waters. *Geophys. Res. Lett.* **44**, 6278–6285 (2017).
8. Osman, M. B. et al. Industrial-era decline in subarctic Atlantic productivity. *Nature* **569**, 551–555 (2019).
9. Abram, N. J. et al. Early onset of industrial-era warming across the oceans and continents. *Nature* **536**, 411–418 (2016).
10. Liu, J. et al. Has Arctic sea ice loss contributed to increased surface melting of the Greenland ice sheet? *J. Clim.* **29**, 3373–3386 (2016).
11. Gardner, A. S. et al. A reconciled estimate of glacier contributions to sea level rise: 2003 to 2009. *Science* **340**, 852–857 (2013).
12. Bolch, T. et al. Mass loss of Greenland’s glaciers and ice caps 2003–2008 revealed from ICESat laser altimetry data. *Geophys. Res. Lett.* **40**, 875–881 (2013).

13. Young, N. E., Schweinsberg, A. D., Briner, J. P. & Schaefer, J. M. Glacier maxima in Baffin Bay during the Medieval Warm Period coeval with Norse settlement. *Sci. Adv.* **1**, e1500806 (2015).
14. Jomelli, V. et al. Paradoxical cold conditions during the medieval climate anomaly in the Western Arctic. *Sci. Rep.* **6**, 32984 (2016).
15. Schweinsberg, A. D. et al. Multiple independent records of local glacier variability on Nuussuaq, west Greenland, during the Holocene. *Quat. Sci. Rev.* **215**, 253–271 (2019).
16. Schweinsberg, A. D., Briner, J. P., Miller, G. H., Bennike, O. & Thomas, E. K. Local glaciation in west Greenland linked to North Atlantic Ocean circulation during the Holocene. *Geology* **45**, 195–198 (2017).
17. Olsen, J., Anderson, N. J. & Knudsen, M. F. Variability of the North Atlantic Oscillation over the past 5,200 years. *Nat. Geosci.* **5**, 808–812 (2012).
18. Millet, L. et al. Anthropogenic versus climatic control in a high-resolution 1500-year chironomid stratigraphy from a southwestern Greenland lake. *Quat. Res.* **81**, 193–202 (2014).
19. Thomas, E. K., Briner, J. P., Ryan-Henry, J. J. & Huang, Y. A major increase in winter snowfall during the middle Holocene on western Greenland caused by reduced sea ice in Baffin Bay and the Labrador Sea. *Geophys. Res. Lett.* **43**, 5302–5308 (2016).
20. Lasher, G. E. & Axford, Y. Medieval warmth confirmed at the Norse Eastern Settlement in Greenland. *Geology* **47**, 267–270 (2019).
21. McConnell, J. R., Lamorey, G. W., Lambert, S. W. & Taylor, K. C. Continuous ice-core chemical analyses using inductively coupled plasma mass spectrometry. *Environ. Sci. Technol.* **36**, 7–11 (2002).
22. Meese, D. A. et al. The accumulation record from the GISP2 core as an indicator of climate change throughout the Holocene. *Science* **266**, 1680–1682 (1994).
23. Hammer, C. U. & Dahl-Jensen, D. *GRIP Accumulation Rates* (PANGAEA, 1999); <https://doi.org/10.1594/PANGAEA.55084>
24. Ebisuzaki, W. A method to estimate the statistical significance of a correlation when the data are serially correlated. *J. Clim.* **10**, 2147–2153 (1997).
25. McKay, N. P. & Kaufman, D. S. An extended Arctic proxy temperature database for the past 2,000 years. *Sci. Data* **1**, 140026 (2014).
26. Badgeley, J. A., Steig, E. J., Hakim, G. J. & Fudge, T. J. Greenland temperature and precipitation over the last 20 000 years using data assimilation. *Clim.* **16**, 1325–1346 (2020).
27. Mernild, S. H. et al. Greenland precipitation trends in a long-term instrumental climate context (1890–2012): evaluation of coastal and ice core records. *Int. J. Climatol.* **35**, 303–320 (2015).
28. Wong, G. J. et al. Coast-to-interior gradient in recent northwest Greenland precipitation trends (1952–2012). *Environ. Res. Lett.* **10**, 114008 (2015).
29. Bintanja, R. & Selten, F. M. Future increases in Arctic precipitation linked to local evaporation and sea-ice retreat. *Nature* **509**, 479–482 (2014).
30. Sodemann, H., Schwierz, C. & Wernli, H. Interannual variability of Greenland winter precipitation sources: Lagrangian moisture diagnostic and North Atlantic Oscillation influence. *J. Geophys. Res. Atmos.* **113**, D03107 (2008).
31. Läderach, A. & Sodemann, H. A revised picture of the atmospheric moisture residence time. *Geophys. Res. Lett.* **43**, 924–933 (2016).
32. Buizert, C. et al. Greenland-wide seasonal temperatures during the last deglaciation. *Geophys. Res. Lett.* **45**, 1905–1914 (2018).
33. Frieler, K. et al. Consistent evidence of increasing Antarctic accumulation with warming. *Nat. Clim. Change* **5**, 348–352 (2015).
34. Cuffey, K. & Paterson, W. S. B. *The Physics of Glaciers* 4th edn (Academic Press, 2010).
35. Trouet, V. et al. Persistent positive North Atlantic Oscillation mode dominated the Medieval Climate Anomaly. *Science* **324**, 78–80 (2009).
36. MacFerrin, M. et al. Rapid expansion of Greenland's low-permeability ice slabs. *Nature* **573**, 403–407 (2019).
37. Fisher, D. et al. Recent melt rates of Canadian Arctic ice caps are the highest in four millennia. *Glob. Planet. Change* **84–85**, 3–7 (2012).
38. Fettweis, X. et al. Important role of the mid-tropospheric atmospheric circulation in the recent surface melt increase over the Greenland ice sheet. *Cryosphere* **7**, 241–248 (2013).
39. Hahn, L., Ummenhofer, C. C. & Kwon, Y.-O. North Atlantic natural variability modulates emergence of widespread Greenland melt in a warming climate. *Geophys. Res. Lett.* **45**, 9171–9178 (2018).
40. Sherman, P., Tziperman, E., Deser, C. & McElroy, M. Historical and future roles of internal atmospheric variability in modulating summertime Greenland Ice Sheet melt. *Geophys. Res. Lett.* **47**, e2019GL086913 (2020).
41. Ortega, P. et al. A model-tested North Atlantic Oscillation reconstruction for the past millennium. *Nature* **523**, 71–74 (2015).
42. Cook, E. R. et al. A Euro-Mediterranean tree-ring reconstruction of the winter NAO index since 910 C.E. *Clim. Dyn.* **53**, 1567–1580 (2019).
43. Lehner, F., Raible, C. C. & Stocker, T. F. Testing the robustness of a precipitation proxy-based North Atlantic Oscillation reconstruction. *Quat. Sci. Rev.* **45**, 85–94 (2012).
44. Gómez-Navarro, J. J. & Zorita, E. Atmospheric annular modes in simulations over the past millennium: no long-term response to external forcing. *Geophys. Res. Lett.* **40**, 3232–3236 (2013).
45. Dahl-Jensen, D. et al. Past temperatures directly from the Greenland ice sheet. *Science* **282**, 268–271 (1998).
46. Kobashi, T. et al. High variability of Greenland surface temperature over the past 4000 years estimated from trapped air in an ice core. *Geophys. Res. Lett.* **38**, L21501 (2011).
47. Sicre, M.-A. et al. Labrador Current variability over the last 2000 years. *Earth Planet. Sci. Lett.* **400**, 26–32 (2014).
48. Björk, A. A. et al. Changes in Greenland's peripheral glaciers linked to the North Atlantic Oscillation. *Nat. Clim. Change* **8**, 48–52 (2018).
49. Pattyn, F. et al. The Greenland and Antarctic ice sheets under 1.5°C global warming. *Nat. Clim. Change* **8**, 1053–1061 (2018).
50. Jones, P. D. et al. Hemispheric and large-scale land-surface air temperature variations: an extensive revision and an update to 2010. *J. Geophys. Res. Atmos.* **117**, D05127 (2012).

Publisher's note Springer Nature remains neutral with regard to jurisdictional claims in published maps and institutional affiliations.

© The Author(s), under exclusive licence to Springer Nature Limited 2021

Methods

Ice core drilling, processing and dating. Drilling was conducted over the span of three days in April 2015 using an 81 mm diameter Eclipse-Badger Drill provided by the US Ice Drilling Program (IDP; formerly Ice Drilling and Design and Operations, IDDO), reaching a (contiguous) bottom depth of 137.97 m below the surface, shy of bedrock (Fig. 2a) due to imposing field work deadlines. Borehole temperature measurements, conducted at ~10 m intervals, indicated an 11.5 m temperature of -6.54°C , stabilizing to between -13.01 and -13.79°C at depths below 41.5 m.

Ice core processing was conducted in June 2015 at the United States Geological Survey's National Ice Core Laboratory (NICL; Lakeland, CO) in a Class-100 HEPA-filtered cold room (-24°C), where the Nuussuaq core was cut into 3 cm \times 3 cm longitudinal sections for chemical analyses. Several complimentary, non-destructive measurements were conducted at NICL, including replicate core density measurements and 1 mm resolution electrical conductivity measurements⁵¹ for volcanic layer identification. The Nuussuaq core was stored for approximately one year at NICL at -34°C before being transported to the Desert Research Institute (DRI; Nevada System of Higher Education). At DRI, chemical analyses were conducted for the entirety of the core over a one-week span in mid-May 2016 using a continuous ice core melter system. Technical aspects of the DRI continuous melter system have been previously described^{21,52}. Measurements conducted at DRI on the Nuussuaq ice core included simultaneous, depth-registered concentration measurements of ten trace species (Na, Mg, S, Cl, Ca, Br, Sr, Ce, Tl and Pb) from two inductively coupled plasma mass spectrometers, water isotope abundances ($\delta^{18}\text{O}$ and δD of H_2O) from a Picarro liquid water laser spectrometer, black carbon concentrations from a single particle soot photometer (SP2, Droplet Measurement Technologies), soluble chemistry (NH_4^+ and HNO_3^-) and conductivity using continuous flow analysis and semi-quantitative particle concentrations using an Abakus particle counter. In total, 17 parameters were measured at continuous ~2 cm water equivalent resolution over the entirety of the core depth. Additionally, 24 low-resolution measurements (~0.2–0.5 m) of ^{239}Pu , a proxy for nuclear weapons testing, were conducted over targeted shallow to mid-depth portions of the core (23–33 m depth⁵³) for dating purposes.

From our chemical and electrical conductivity measurements, it was possible to identify 55 age-constrained tie-points over the span of the core length (Supplementary Table 1). These tie-points reference 20th century radiogenic bomb horizons (2 ties; identified via ^{239}Pu (ref. ⁵³)), volcanic eruptions (49 ties, identified primarily via non-sea-salt sulfur and electrical conductivity) and anthropogenically sourced heavy-metallic emissions (4 ties based on Pb (ref. ⁵²)). The shallowest ~90 m of the core (~2/3 of the core depth), down to the Huaynaputina (Peru) volcanic eruption reference horizon at 1601 CE (ref. ⁵⁴), contains the best-dated portion of the core (<2 year relative uncertainty), as vertical strain and associated thinning of annual layers have not yet become severe as to preclude the identification of seasonality in most chemical parameters (Fig. 2b). In deeper portions of the core, where seasonality in chemical parameters could no longer be adequately discriminated, dating relied on an iterative synchronization of well-prescribed volcanic⁵⁴ and heavy-metal horizons⁵² to alternate well-dated inland GrIS cores (for example, NGRIP2 and NEEM-2011-S1; Extended Data Fig. 2) following the procedure outlined by McConnell et al.⁵². Although it is a semi-subjective approach, we consider age-defined tie-points down to the 536 CE mega-eruption horizon (ref. ⁵⁴; 132.64 m) to be well constrained ($1\sigma \leq 5$ years) given this portion of the NU record's sufficient sampling time resolution (>1 sample per year) and the multi-parameter approach used for tie-point synchronization (Extended Data Fig. 2 and Supplementary Table 1). Due to severe thinning of annual layers below 132.64 m (Fig. 2), the identification of tie-points in the deepest ~3 metres of core relied most intensively on 1 mm resolution alternating-current electrical conductivity measurements (Extended Data Fig. 2b) synchronized to the aforementioned interior GrIS ice core records⁵⁴. Below the 536 CE horizon, relative uncertainty is estimated to $1\sigma = 10$ years at 424 CE, increasing to $1\sigma = 50$ years at 169.5 CE, the deepest age horizon identified.

Ice cap strain forward model. The physical setting of the NU ice cap is advantageous for understanding past GIC-climatic interactions. First, the steep promontory on which the ice cap rests sets a natural upper limit on its areal coverage, while likely also moderating associated changes in ice thickness under variable climate conditions. Second, the smoothness of the underlying bed topography (determined from a combination of ground-based ice penetrating radar and a digital elevation model derived from Worldview satellite stereo imagery⁵⁵; Fig. 2 and Supplementary Sections 1–3) suggests that relatively simple glacial flow conditions prevail at the NU ice cap³⁴; this suggestion is further supported by borehole temperature measurements showing static cold-based thermal conditions persisting throughout the NU core depth below the pore close-off depth (~40 m). Given these facts, we take the relatively simple case in which our forward one-dimensional ice strain model (encapsulated in equation (1) as $G(\mathbf{m})$) assumes a linear increase in vertical shear stress with depth and no basal melting, closely following Nye³⁶. The primary advantage of this conceptual model is that only knowledge of the site-mean surface vertical velocity (that is, climatological accumulation rate) and ice cap thickness are required as initial conditions for inferring the shape profile of ice flow vertical velocity, thus

permitting low computational expense and better constrained (that is, fewer unknowns) inversions. However, we acknowledge that more complicated ice flow models could also be used (see, for example, Fudge et al.⁵⁷). A full numerical treatment can be found in Supplementary Section 5.

Nu moisture source tracking. We quantified seasonal and interannual variations in the evaporative moisture sources leading to precipitation over the Nuussuaq Peninsula (target area 55.3°W to 49.3°W , 69.5°N to 71.5°N) using the WaterSip method^{30,58}. In the present study, we used the dataset of Läderach and Sodemann³¹, where trajectories are extracted from a global simulation of 5 million particles that are advected continuously with the Lagrangian particle dispersion model FLEXPART⁵⁹. Air parcel trajectories were computed using winds from the European Centre for Medium-Range Weather Forecasts (ECMWF) ERA-Interim reanalysis⁶⁰ at $1^{\circ} \times 1^{\circ}$ horizontal resolution over 60 vertical levels during the period 1980–2013 CE, with additional variables interpolated to the trajectory positions. Moisture gains (evaporation) or losses (presumed to represent precipitation only if losses were >0.10 mm per 6 h) were evaluated along a given trajectory by tallying the specific humidity content of that air parcel. Using this method, the percentage of explained moisture contained in a given air parcel at each successive time step could be quantified through a mass-weighted summing of evaporation and precipitation events along that air parcel's trajectory. The WaterSip method captures the large majority of moisture uptake in an airmass, while underestimating the (typically small) contribution of very long-lived water vapour⁵⁸. By budgeting across successive years, the relative source contribution of precipitated moisture over the NU ice cap could be allocated on a grid-by-grid basis, a spatial diagnostic that in turn allowed for straightforward determination of accompanying temporal diagnostics such as moisture source temperature (for example, Extended Data Figs. 7 and 9a).

Data availability

Ice core annual accumulation time series (Figs. 3 and 4) are publicly available via the National Oceanic and Atmospheric Administration (NOAA) Paleoclimatology Data Archive (<https://www.ncdc.noaa.gov/paleo/study/33772>). Depth-resolved geochemical and ice-conductivity measurements, used for time-dating of the NU ice core (for example, S, Pb, Tl, Mg and Na), are available via the National Science Foundation Arctic Data Center (<https://arcticdata.io>). NASA Operation IceBridge data (Fig. 2a and Supplementary Section 2) can be accessed using the National Snow and Ice Data Center's (NSIDC) IceBridge Data Portal (<https://nsidc.org/icebridge/portal/map>). Temperature reanalysis data (Fig. 4) from HadCRUT4 are available from <https://crudata.uea.ac.uk/cru/data/temperature/>. WaterSip data are available from H.S. on request.

Code availability

Ice strain inversion source code is available at <https://github.com/mattosman/NU-inversion>. Code for post-processing and analysis of WaterSip data, and all associated statistical analyses described herein, is available from M.B.O. on request.

References

- Taylor, K. et al. Ice-core dating and chemistry by direct-current electrical conductivity. *J. Glaciol.* **38**, 325–332 (1992).
- McConnell, J. R. et al. Pervasive Arctic lead pollution suggests substantial growth in medieval silver production modulated by plague, climate, and conflict. *Proc. Natl. Acad. Sci. USA* **116**, 14910–14915 (2019).
- Arienzo, M. M. et al. A method for continuous ^{239}Pu determinations in Arctic and Antarctic ice cores. *Environ. Sci. Technol.* **50**, 7066–7073 (2016).
- Sigl, M. et al. Timing and climate forcing of volcanic eruptions for the past 2,500 years. *Nature* **523**, 543–549 (2015).
- Shean, D. E. et al. An automated, open-source pipeline for mass production of digital elevation models (DEMs) from very-high-resolution commercial stereo satellite imagery. *ISPRS J. Photogramm. Remote Sens.* **116**, 101–117 (2016).
- Nye, J. F. Correction factor for accumulation measured by the thickness of the annual layers in an ice sheet. *J. Glaciol.* **4**, 785–788 (1963).
- Fudge, T. J., Waddington, E. D., Conway, H., Lundin, J. M. D. & Taylor, K. Interpolation methods for Antarctic ice-core timescales: application to Byrd, Siple Dome and Law Dome ice cores. *Clim* **10**, 1195–1209 (2014).
- Sodemann, H. Beyond turnover time: constraining the lifetime distribution of water vapor from simple and complex approaches. *J. Atmos. Sci.* **77**, 413–433 (2019).
- Stohl, A. & James, P. A Lagrangian analysis of the atmospheric branch of the global water cycle. Part II: moisture transports between Earth's ocean basins and river catchments. *J. Hydrometeorol.* **6**, 961–984 (2005).
- Dee, D. P. et al. The ERA-Interim reanalysis: configuration and performance of the data assimilation system. *Q. J. R. Meteorol. Soc.* **137**, 553–597 (2011).
- Axford, Y. et al. Holocene temperature history at the western Greenland Ice Sheet margin reconstructed from lake sediments. *Quat. Sci. Rev.* **59**, 87–100 (2013).

62. Anderson, N. J., Liversidge, A. C., McGowan, S. & Jones, M. D. Lake and catchment response to Holocene environmental change: spatial variability along a climate gradient in southwest Greenland. *J. Paleolimnol.* **48**, 209–222 (2012).
63. D'Andrea, W. J., Huang, Y., Fritz, S. C. & Anderson, N. J. Abrupt Holocene climate change as an important factor for human migration in west Greenland. *Proc. Natl Acad. Sci. USA* **108**, 9765–9769 (2011).
64. Perren, B. B., Anderson, N. J., Douglas, M. S. V. & Fritz, S. C. The influence of temperature, moisture, and eolian activity on Holocene lake development in west Greenland. *J. Paleolimnol.* **48**, 223–239 (2012).
65. Willemse, N. W. & Törnqvist, T. E. Holocene century-scale temperature variability from west Greenland lake records. *Geology* **27**, 580–584 (1999).
66. Andresen, C. S., Björck, S., Bennike, O. & Bond, G. Holocene climate changes in southern Greenland: evidence from lake sediments. *J. Quat. Sci.* **19**, 783–795 (2004).
67. Poli, P. et al. ERA-20C: an atmospheric reanalysis of the twentieth century. *J. Clim.* **29**, 4083–4097 (2016).
68. Jones, P. D., Jonsson, T. & Wheeler, D. Extension to the North Atlantic oscillation using early instrumental pressure observations from Gibraltar and south-west Iceland. *Int. J. Climatol.* **17**, 1433–1450 (1997).
69. Vinther, B. M., Andersen, K. K., Jones, P. D., Briffa, K. R. & Cappelen, J. Extending Greenland temperature records into the late eighteenth century. *J. Geophys. Res. Atmos.* **111**, D11105 (2006).
70. Abram, N. J. et al. Early onset of industrial-era warming across the oceans and continents. *Nature* **536**, 411–418 (2016).
71. Cappelen, J. *Greenland—DMI Historical Climate Data Collection 1784–2017* DMI Report 18-04 (Danish Meteorological Institute, 2018).
72. Thomas, E. K., McGrane, S., Briner, J. P. & Huang, Y. Leaf wax $\delta^{2}\text{H}$ and varve-thickness climate proxies from proglacial lake sediments, Baffin Island, Arctic Canada. *J. Paleolimnol.* **48**, 193–207 (2012).
73. Compo, G. P. et al. The twentieth century reanalysis project. *Q. J. R. Meteorol. Soc.* **137**, 1–28 (2011).
74. Lenssen, N. J. L. et al. Improvements in the uncertainty model in the Goddard Institute for Space Studies Surface Temperature (GISSTEMP) analysis. *J. Geophys. Res. Atmos.* **124**, 6307–6326 (2019).
75. Ortega, P. et al. A model-tested North Atlantic Oscillation reconstruction for the past millennium. *Nature* **523**, 71–74 (2015).
76. Rayner, N. A. Global analyses of sea surface temperature, sea ice, and night marine air temperature since the late nineteenth century. *J. Geophys. Res.* **108**, 4407 (2003).

Acknowledgements

Funding for retrieval and analysis of the NU ice core was provided by the US National Science Foundation (NSF) Arctic System Science Program award OPP-1205196 to S.B.D. and ARC-1205062 to B.E.S. Geospatial support for this work was provided by the Polar Geospatial Center under NSF-OPP awards 1043681 and 1559691. M.B.O. acknowledges support from the US Department of Defense National Defense Science and Engineering Graduate fellowship and an Ocean Outlook Fellowship to the Bjerknes Centre for Climate Research. L.D.T. acknowledges support from the NSF (grant no. 2021699). H.S. acknowledges support from UNINETT Sigma2 (the National Infrastructure for High Performance Computing and Data Storage in Norway; grant no. NS9054K) and the Norwegian Research Council (grant no. 262710). We thank IDDO and IDPO and M. Waszkiewicz for assistance with ice coring equipment and drilling, Polar Field Services for field support and Air Greenland for air support. We thank the students and staff of the DRI ice core group for laboratory assistance; T.J. Fudge for assistance with electrical conductivity measurements and the NSF Ice Core Facility, A. York, M. Bingham and M. Hatch for Nuussuaq ice core sampling, processing and analysis support.

Author contributions

M.B.O. designed the study with input from B.E.S., L.D.T. and S.B.D.; B.E.S. and S.B.D. determined the Nuussuaq ice cap site location and M.B.O., L.D.T. and S.B.D. collected and processed the NU ice core. M.B.O., J.R.M., N.C. and M.A. analysed the NU ice core chemistry. NU ice core dating was led by M.B.O., B.E.S. designed the ice strain inversion with input from M.B.O., and H.S. conducted the NU ice cap moisture source analysis. Data analysis and interpretation were led by M.B.O., who wrote the manuscript with input from B.E.S., L.D.T. and S.B.D. All authors read and commented on the manuscript.

Competing interests

The authors declare no competing interests.

Additional information

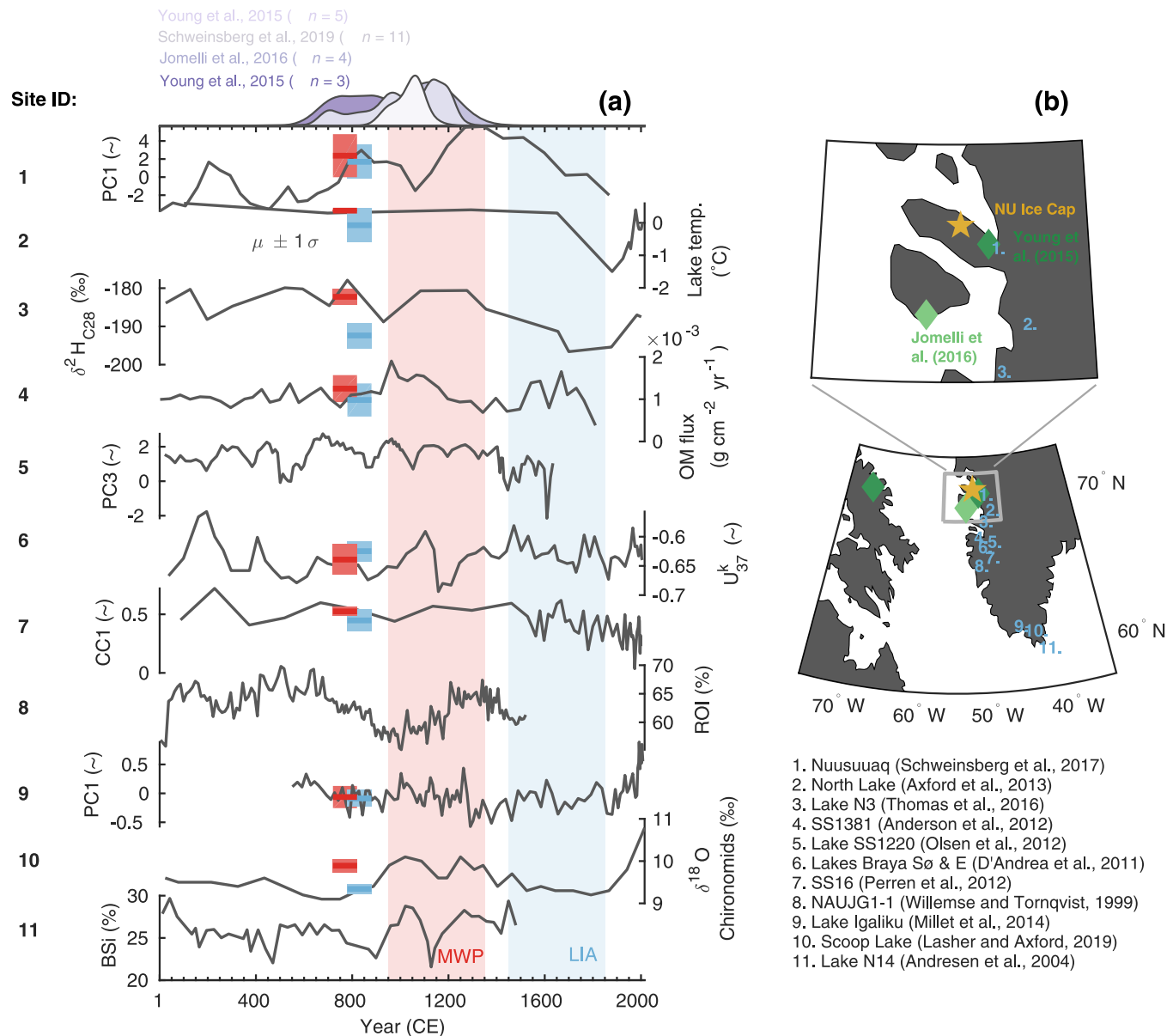
Extended data is available for this paper at <https://doi.org/10.1038/s41561-021-00818-w>.

Supplementary information The online version contains supplementary material available at <https://doi.org/10.1038/s41561-021-00818-w>.

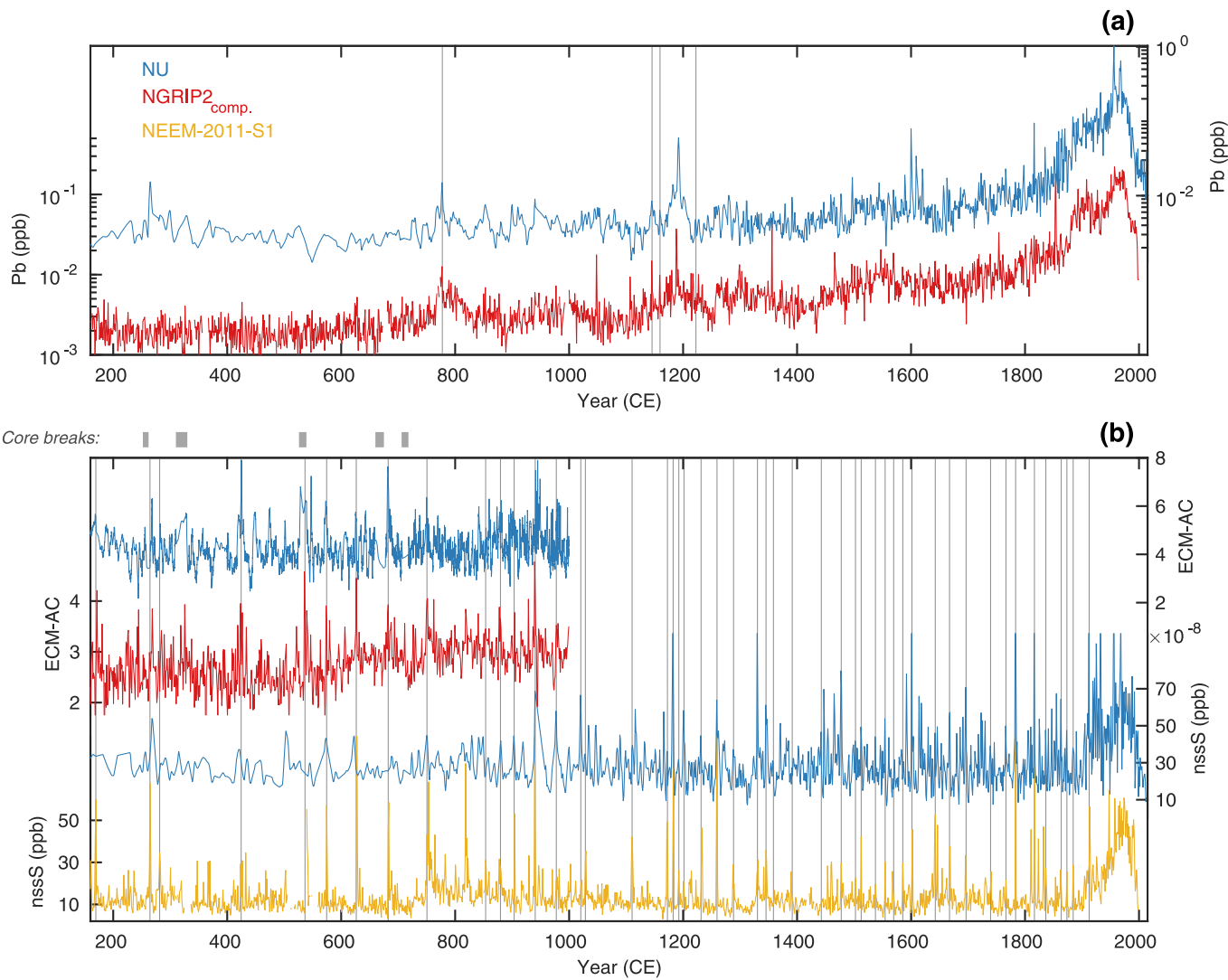
Correspondence and requests for materials should be addressed to Matthew B. Osman.

Peer review information *Nature Geoscience* thanks Joshua Cuzzone, Horst Machguth and the other, anonymous, reviewer(s) for their contribution to the peer review of this work. Primary Handling Editor(s): James Super.

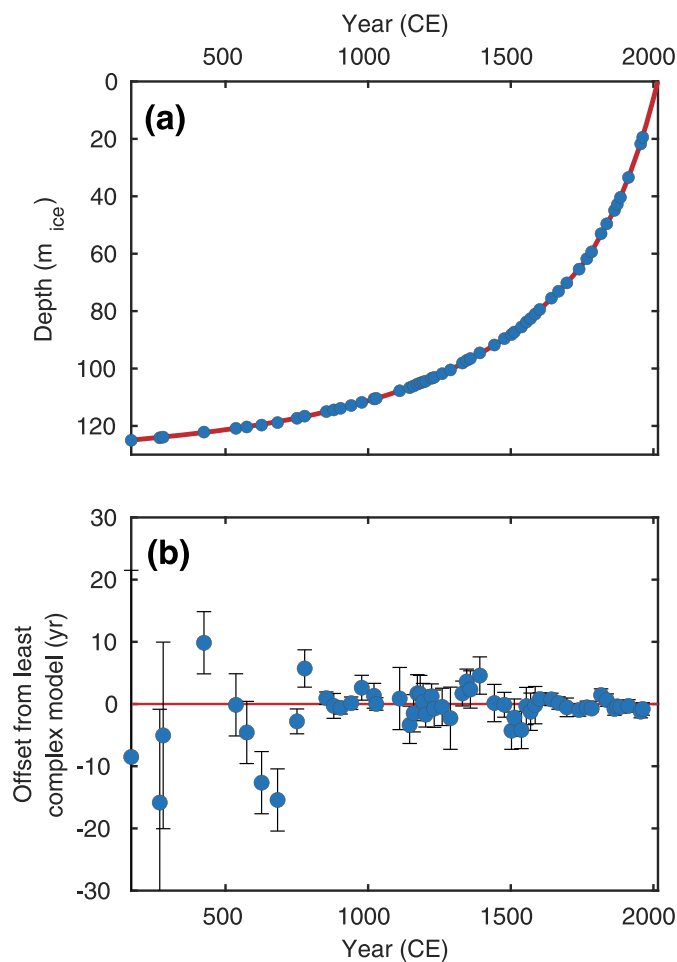
Reprints and permissions information is available at www.nature.com/reprints.



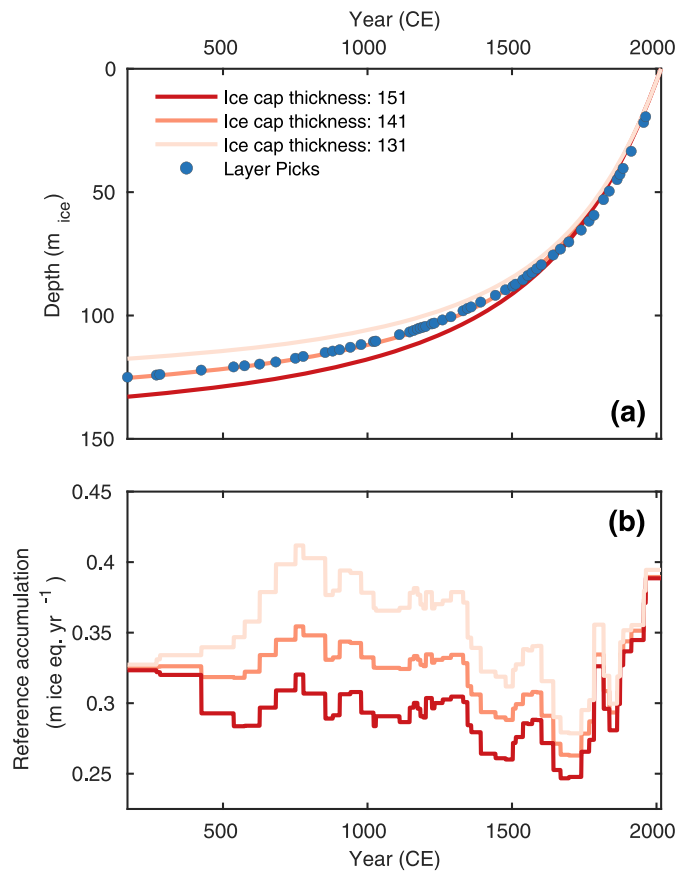
Extended Data Fig. 1 | Comparison of coastal West Greenland terrestrial temperature proxies. **a**, Sediment core-derived time series (all shown with positive orientation relative to increasing temperature) are numbered from 1–11, representing most-northerly to most-southerly situated, with corresponding coastal locations shown in **(b)**. All sediment records are limited to sites containing at least 10 data points during the Common Era. **(1)** First Principal Component (“PC1”) of physical properties measured from the Sikiuu Lake sediment core¹⁶. **(2.)** Reconstructed July lake temperatures from chironomid-abundance assemblages from North Lake, CWG (ref. ⁶¹). **(3.)** Lake N-3 $\delta^{2\text{H}}$ of C₂₈ n-alkanoic acids, produced by terrestrial plants¹⁹. **(4.)** Organic matter (OM) fluxes for SS1381 (ref. ⁶²). **(5.)** PC3 of parameters reflecting lake-bottom redox variability (Mn, Mn/Fe, Ca/Ti and grey scale; ref. ¹⁷). **(6.)** Alkenone unsaturation (U_{37}^K) from Braya Sø⁶³. **(7.)** First canonical correspondence (CC1) of SS16 diatom assemblages⁶⁴. **(8.)** Residue-on-ignition (ROI) from the NAUJG1-1 lake sediment core⁶⁵. **(9.)** Pollen flux to Lake Igaliuk, CWG¹⁸. **(10.)** Scoop Lake temperatures via the $\delta^{18}\text{O}$ content of chironomids²⁰. **(11.)** Biogenic silica abundances in Lake N14 (ref. ⁶⁶). Red and blue ranges represent the mean (μ) and standard deviation (σ) range of MWP (red) and LIA (blue) values. Purple probability density functions at top show outlet glacier distal-moraine age-estimates (where “distal” refers to the most advanced Common Era glacier terminus positions identified at each site) from Nuussuaq Peninsula, Disko Island, and Baffin Island^{13–15}.



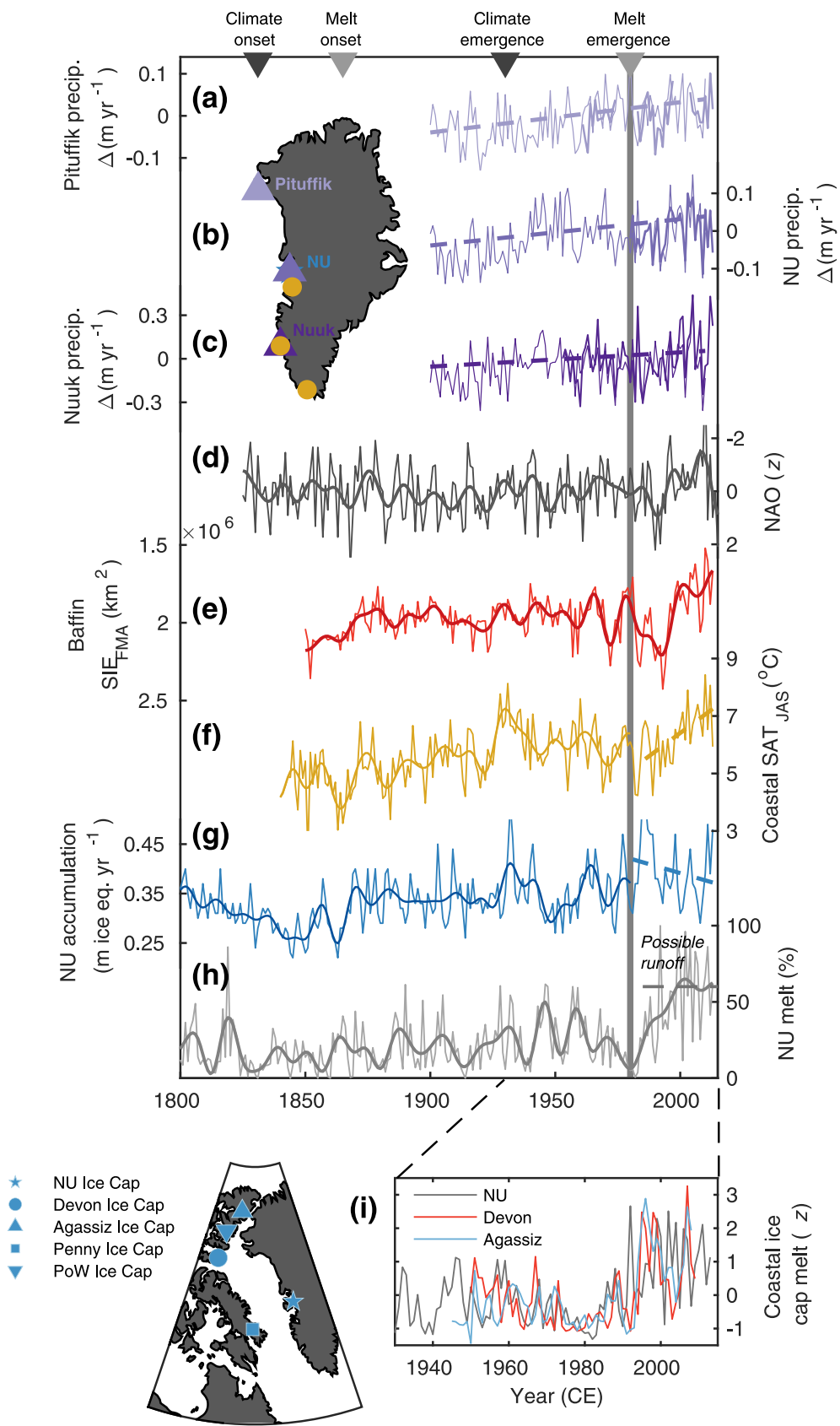
Extended Data Fig. 2 | Synchronization of the Nuussuaq ice core to previously published, well-dated interior Greenland Ice Sheet ice core geochemical records. Shown for comparison alongside the NU record is the NGRIP2_{comp.} (NGRIP2 prior to 1257 CE, composited to NEEM-2011-S1 record thereafter; ref. ⁵²) and NEEM-2011-S1 records for (a) Pb and (b) non-sea-salt sulfur (nssS). Alternating-current Electrical Conductivity Measurements (ECM-AC), conducted at high-resolution (1 mm) along the NU core profile, are shown for the deepest (oldest) portion of the core alongside NGRIP2 ECM measurements⁵² and NEEM-2011-S1 nssS (ref. ⁵⁴). Tie point ages identified along the core length are shown as vertical grey lines. Age scales for the NGRIP2 and NEEM-2011-S1 records follow ref. ⁵².



Extended Data Fig. 3 | Minimized age-constraint offsets in the least complex Nuussuaq age-model. **a**, Recovered age-depth scale for the least complex accumulation history model, alongside the corresponding age-depth picks. Error bars on the age-depth picks, and differences with the recovered age-depth model, is not visible at this scale. **b**, Age differences between the least complex recovered age-depth scale and the age-depth constraints (circles with bars), with the prescribed relative uncertainties shown as the vertical bars.

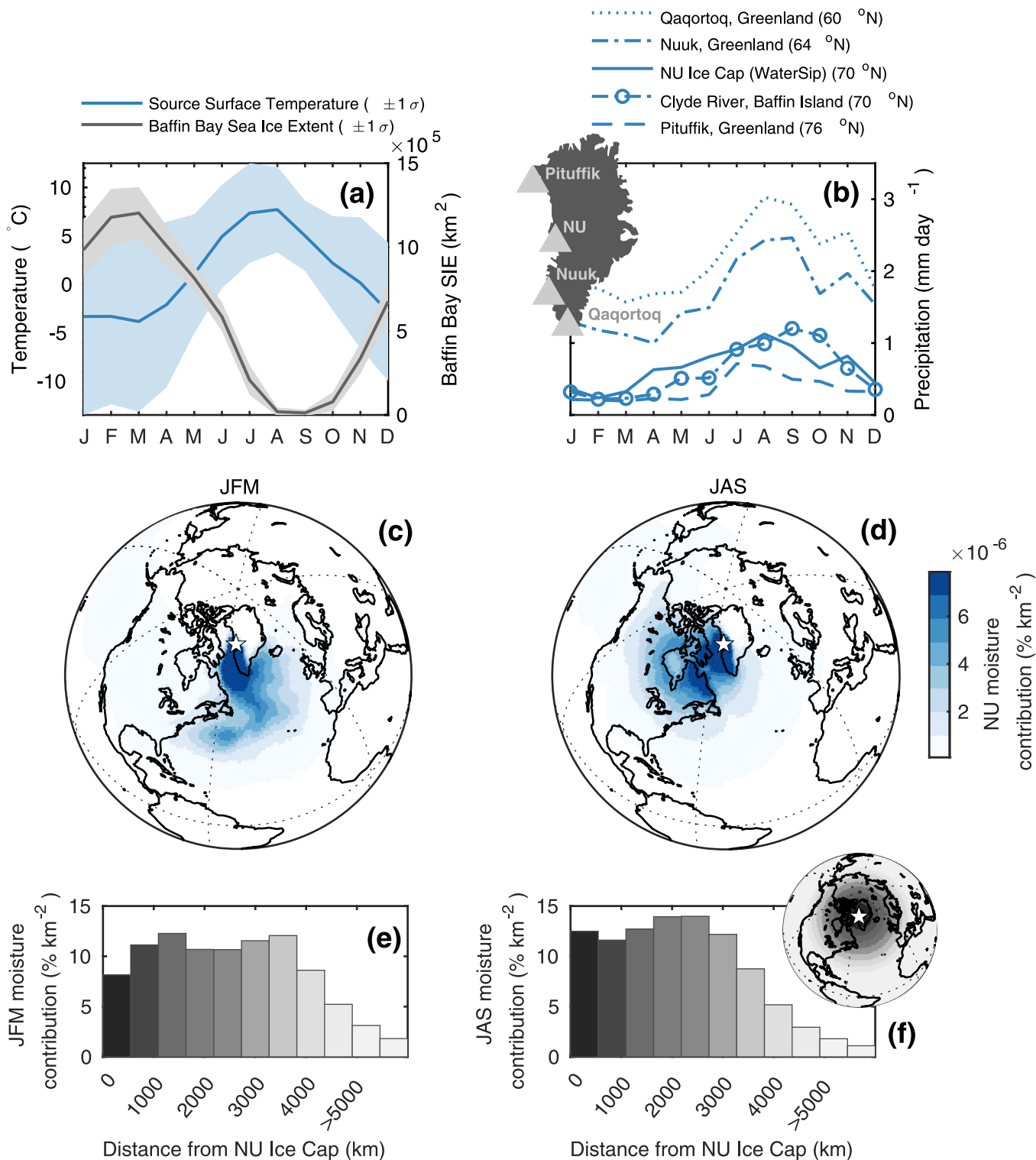


Extended Data Fig. 4 | Consistent Nuussuaq ice cap accumulation histories under varying prescribed reference ice thicknesses and accumulation rates. **a**, Predicted (that is, forward modeled) age-depth scales under three different reference ice thickness ($H_0 = H_{opt} = 141 \text{ } m_{ice}$ and $H_0 = H_{opt} \pm 10 \text{ } m_{ice}$) scenarios and a constant reference accumulation rate ($b_0 = b_{opt} = 0.325 \text{ } m_{ice} \text{ yr}^{-1}$). The depth-age-constraints (“Layer Picks”, Fig. 2b) are shown for comparison, showing all corresponding age-scales agree well at shallow depths, but diverge noticeably at depths greater than approximately $100 \text{ } m_{ice}$ where large variations in depth-ages are increasingly dictated by small variations in ice strain. **b**, Recovered NU accumulation histories estimates for the three model-predicted age-depth scales shown in (a), illustrating the sensitivity of our NU accumulation history to H_0 . For $H_0 = 131 \text{ } m_{ice}$, accumulation rate must increase over much of the core’s time-history to compensate for the added strain implied by the thinner ice cap. The converse is true for $H_0 = 151 \text{ } m_{ice}$, where the annual layers must be relatively thin to compensate for lower strain. The deviations from the global optimum accumulation rate for $H_0 = 131 \text{ } m_{ice}$ and $H_0 = 151 \text{ } m_{ice}$ each imply enhanced model complexity although, importantly, the form of variability over the last millennium appears robust across all models.

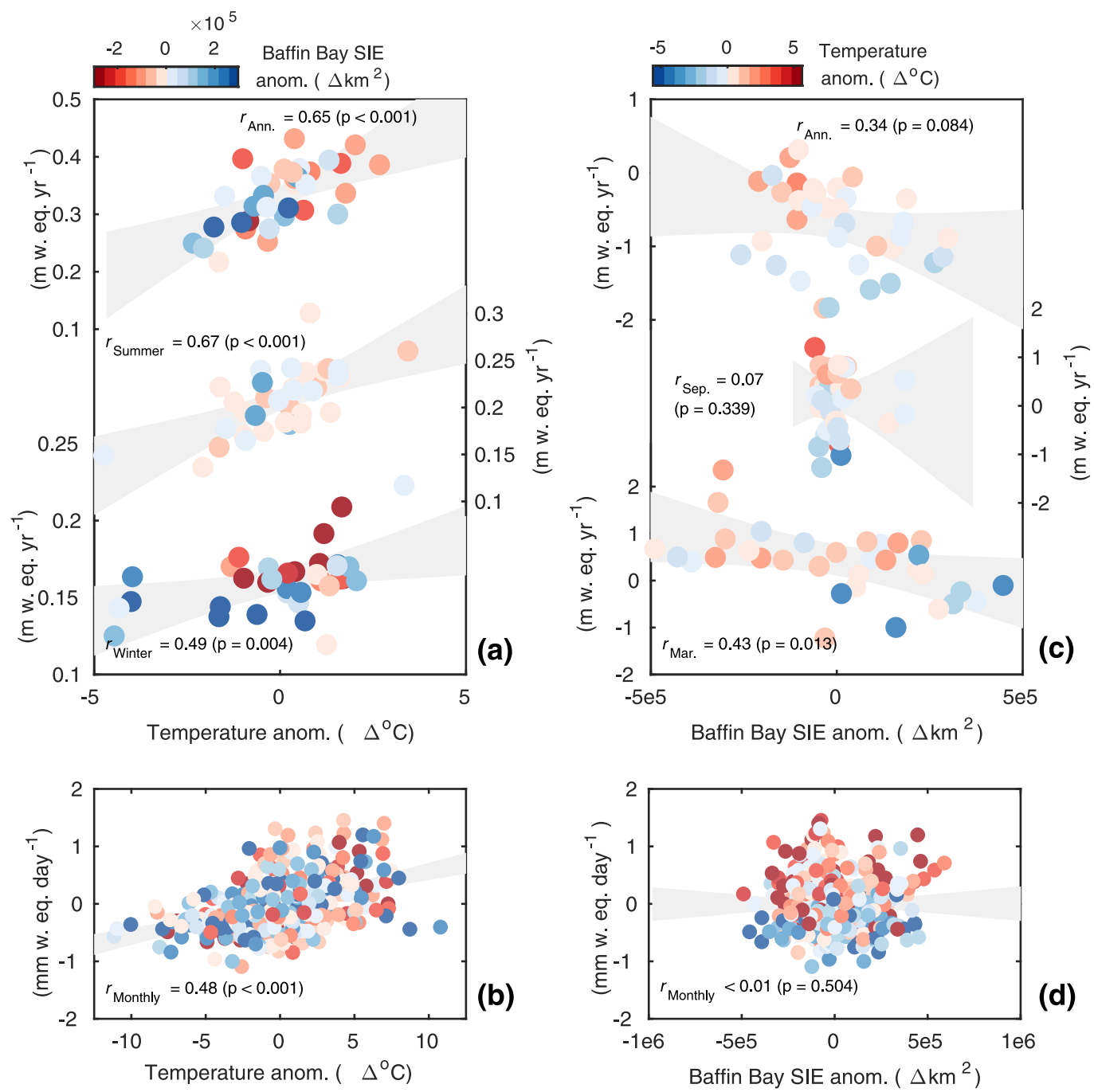


Extended Data Fig. 5 | See next page for caption.

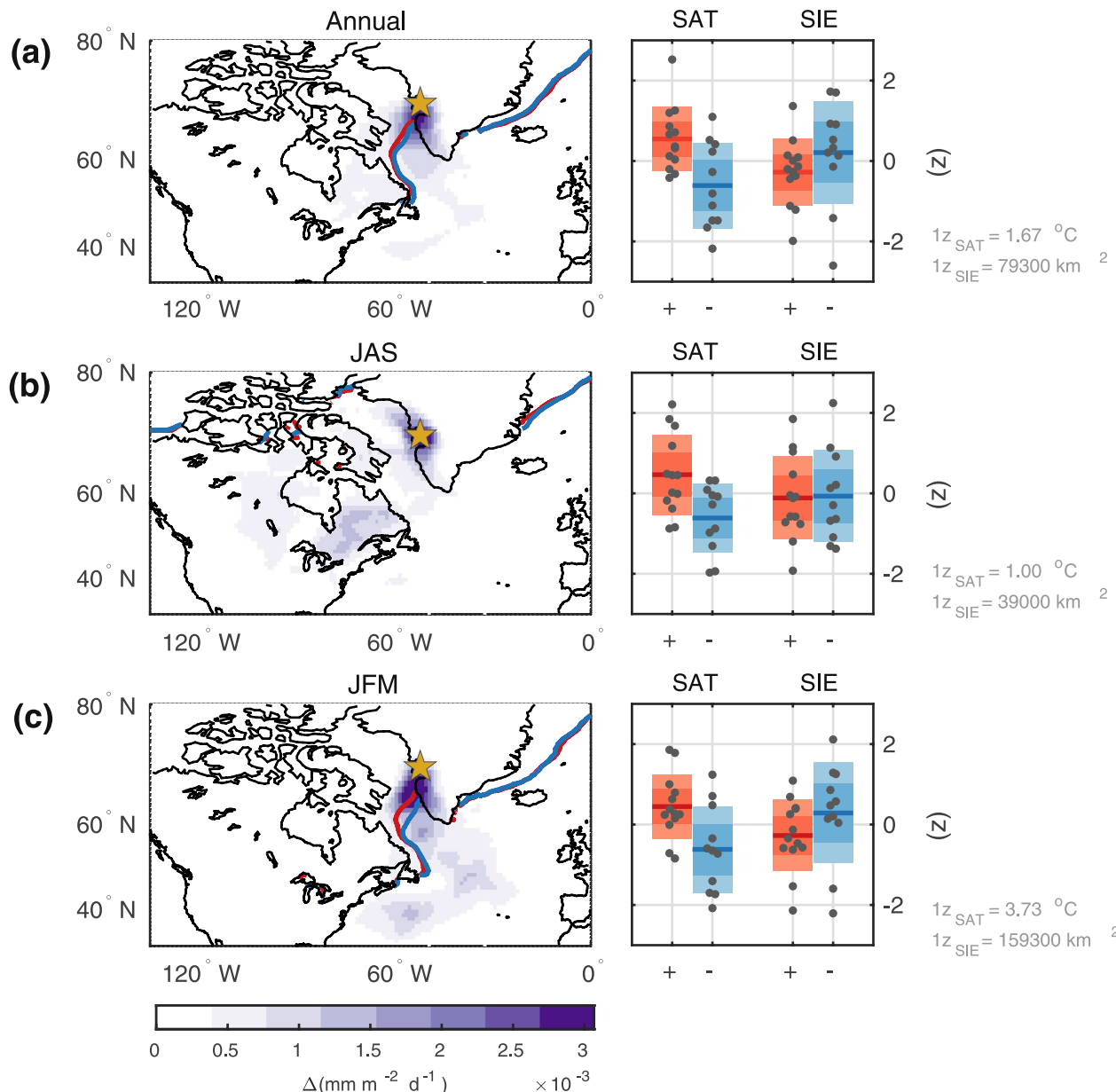
Extended Data Fig. 5 | Industrial-era time series analysis of coastal West Greenland hydroclimate variability. **a**, Danish Meteorological Institute-derived precipitation anomalies at Pituffik and Nuuk compared to (b) WaterSip-inferred NU ice cap precipitation anomalies. Thin lines show precipitation from the ERA-20C reanalysis⁶⁷, illustrating long term increasing CWG trends. **d**, Station-based mean-annual NAO index⁶⁸. **e**, Baffin Bay wintertime (FMA) sea ice extent ("SIE"; 40–80°N, 80–45°W). **f**, Danish Meteorological Institute-derived summertime CWG temperatures from ref. ⁶⁹ (note site locations in the inset). **g**, The NU annual-resolution accumulation history and (h) melt percent history. Panel (i) shows overlapping annual resolution Devon and Agassiz Ice Cap melt histories alongside NU melt, with site locations for time series shown here and in Fig. 4d at left for reference. All annual and 10-yr lowpass filtered data are shown using thin and thick lines, respectively. Shown at top for comparison is the estimated industrial-era onset and emergence timing of Arctic temperature⁷⁰ and CWG melt (light grey; ref. ²). Note the strong covariation ($r = 0.69$; $p < 0.001$) between NU mass balance and coastal summertime temperatures prior to local melt-emergence.



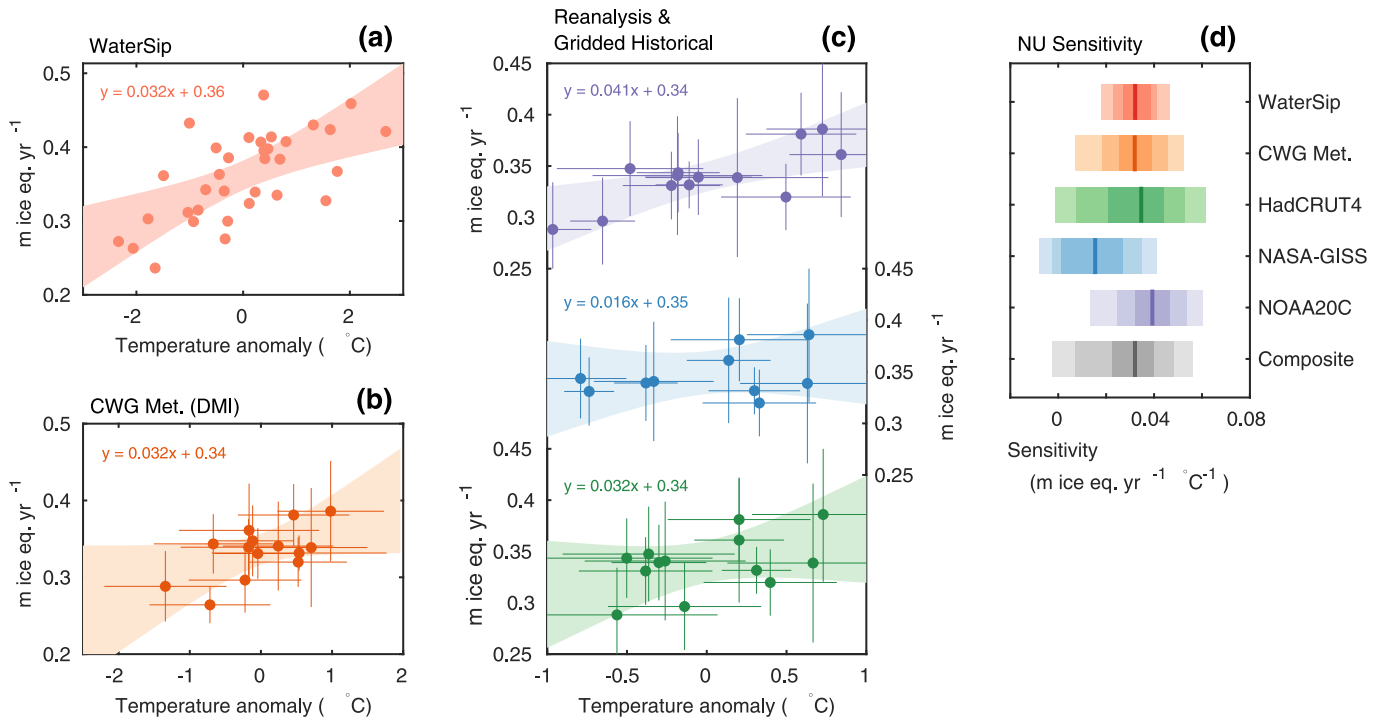
Extended Data Fig. 6 | Seasonal moisture source estimates for the Nuussuaq Ice Cap. **a**, The WaterSip-diagnosed seasonal cycle of moisture-source 2 m surface air temperature (yellow) and Baffin Bay (defined $85\text{--}45^{\circ}\text{W}$ and $40\text{--}80^{\circ}\text{N}$) sea ice extent from ERA-Interim during the same period (“SIE”; grey). Thick lines denote the mean and shaded bands the 1σ range. **b**, WaterSip-estimated NU precipitation seasonality (median ± 1 median-absolute-deviation) based on ERA-Interim precipitation⁶⁰. Also shown are monthly precipitation rates from the Danish Meteorological Institute⁷¹ weather-stations in Nuuk (64°N), Qaqortoq (60°N) and Pituffik (76°N ; see also inset Greenland map to the right of (b)). Clyde River data are from ref. ⁷². **c**, Percent contribution of the NU annual moisture budget per degree latitude-longitude, inferred from WaterSip (Section 6.2) during January–February–March (JFM; CWG precipitation minimum). **d**, As in (c), but for July–August–September (JAS; CWG precipitation maximum). **e** and **f**: Percent moisture contribution as a function of distance from the NU ice core site, shown for JFM and JAS, respectively (see also Fig. 1b–c). Bar plots in (e) and (f) and inset globe to the right of (f), are color-coded by distance from the NU ice core site.



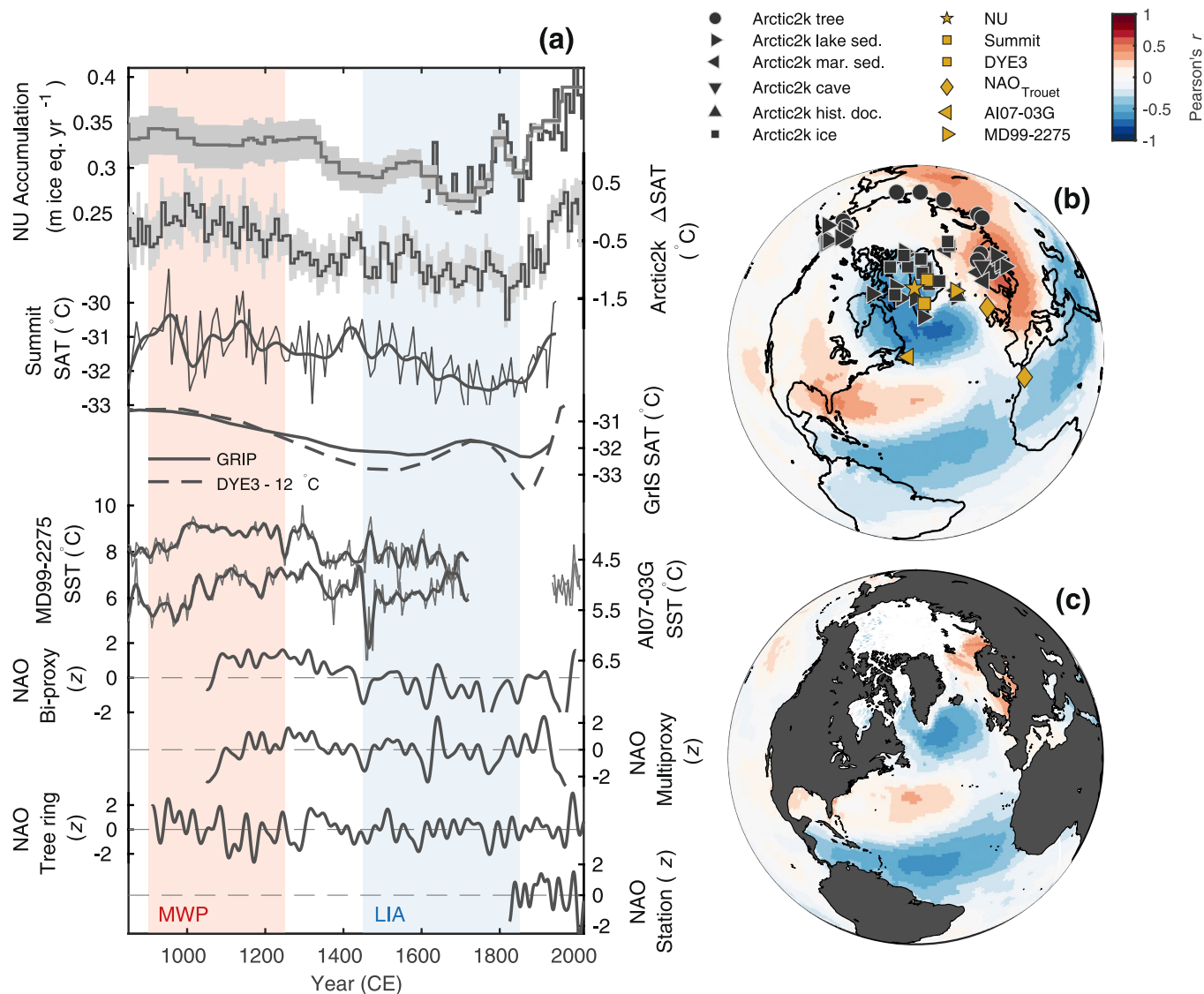
Extended Data Fig. 7 | Relationships between WaterSip-modeled Nuussuaq precipitation and moisture source temperature (a-b) and Baffin Bay sea-ice extent (SIE) (c-d) at mean-annual (a,c) and mean-monthly (b,d) resolutions. Points in (a) are color-coded with respect to Baffin SIE (1980–2013 CE), and in (b) with respect to moisture source temperature (1980–2013 CE). All monthly anomalies have been seasonally detrended. Both linear correlations shown in (a) are significant at $p < 0.0001$ via the method of ref. ²⁴. Note different x-scales in the top vs. bottom panels.



Extended Data Fig. 8 | Mean-annual, summertime, and wintertime Nuussuaq precipitation sensitivity to temperature and sea-ice changes. Shown in the left panels are WaterSip-diagnosed (a) annual, (b) JAS, and (c) JFM NU evaporation-rate differencing maps for years with anomalously high- vs. low snowfall accumulation over the NU ice cap. Anomalous snow accumulation years are defined as years when model-estimated snowfall deviates greater than 0.5σ and less than -0.5σ , where σ denotes transformation to z-score units relative to the observational period 1980–2013 CE. Red and blue lines shown in the left panel denote the corresponding mean sea ice edge position (defined as the 15% sea ice concentration isopleth) for all anomalously high and low NU snow-accumulation years, respectively. The right panels denote the corresponding SW Greenland temperature⁶⁹ and Baffin Bay (defined 40–80°N, 80–45°W) sea ice extent (SIE) anomalies (shown in z-score units for visualization) for anomalously high (red) and low (blue) NU snow-accumulation years. Box plot center lines denote the mean, dark shading the $\pm 1\sigma$ range, and light shading the 95% confidence interval. Collectively, the results suggest that although temperature is most important in dictating NU snow accumulation on a year-round basis, Baffin Bay SIE may also play a non-negligible secondary role by dictating wintertime NU snow-accumulation.



Extended Data Fig. 9 | Sensitivity of modelled and observed Nuussuaq accumulation changes to temperature. **a**, WaterSip precipitation sensitivity to moisture source temperature. **b**, NU accumulation vs. CWG Danish Meteorological Institute⁷¹ mean annual surface temperature. **c**, Observed NU accumulation sensitivity to three different pan-Arctic surface air temperature estimates: the NOAA 20th Century Reanalysis (NOAA20C; ref. ⁷³), the NASA-GISS product⁷⁴, and the HadCRUT4 product⁵⁰. Analyzed values in (b) and (c) are 10-yr mean-binned resolution, ignoring the most-recent post-1980 GIC melt-emergence period. All dependent- and independent-variable uncertainties are $\pm 1\sigma$ ($n = 10$ years) and the shaded bands the 95% confidence intervals of the weighted regression. **d**, Bootstrap-derived (random sampling with replacement; $n = 1,000$ iterations) sensitivity of NU accumulation per degree warming. Confidence ranges are, from lightest to darkest, 2.5–97.5th, 10–90th, 25–75th, and 50th percentiles.



Extended Data Fig. 10 | Comparison of regional temperature and the North Atlantic Oscillation during the Common Era. **a**, From top: comparison of NU ice core accumulation (this study) against Arctic-2k temperature²⁵; ice core $\delta^{15}\text{N}$ - $\delta^{40}\text{Ar}$ gas-derived surface air temperature⁴⁶; interior Greenland ice core borehole thermometer-derived surface air temperatures⁴⁵; alkenone-based sea-surface temperature from MD99-2275 and A07-036 (inverted y-axis) showing divergent MWP warming/cooling, respectively⁴⁷; a bi-proxy (Scotland speleothem and Moroccan tree ring) NAO reconstruction³⁵; a multiproxy model-tested NAO reconstruction⁷⁵; a tree-ring based NAO reconstruction⁴²; and a station-based NAO index⁶⁸. All NAO series are shown at 30-yr lowpass resolution for visual comparison. Vertical light red and blue shaded intervals are the MWP and LIA, respectively. Panels (b) and (c) show spatial correlation maps (1900–2015 CE) for the mean annual NAO index of ref. ⁶⁸ vs. NOAA20C mean annual surface air temperatures (SAT)⁷³ and HadISST v1.1 mean annual sea surface temperature (SST)⁷⁶, respectively. Site locations from (a) are highlighted in (b); note the predominance of Baffin Bay-centric sites from the Arctic-2k compilation²⁵.